Indian Journal of Pure & Applied Physics
Vol. 62, November 2024, pp. 961-970
DOI: 10.56042/ijpap.v62i11.6491

Uniformity-based Magnetic Field and Improvement of Conversion Efficiency for Rotary Ultrasonic Machining Applications

Rui Yang[a*], Zhenxing Hao[a], Xiaojing Hu[a] & Yunshuai Chen[b]

[a]School of Mechanical Engineering, Zhengzhou University of Science and Technology, Zhengzhou 450 064, China

[b]School of Mechanical and Precision Instrument Engineering, Xi'an University of Technology, Xi'an 710 048, China

Received 10 November 2023; accepted 10 October 2024

A giant magnetostrictive transducer is a highly integrated device that facilitates the conversion of magnetic energy into mechanical energy, enabling the generation of motion or force during actuation. However, the energy efficiency of giant magnetostrictive materials (GMM) is hindered by several factors, resulting inless-than-optimal performance. To improve energy conversion efficiency, a magnetic circuit control strategy for optimizing the transducer is proposed, focusing on increasing magnetic flux density and enhancing magnetic field uniformity. Theoretical derivations demonstrate the positive correlation between magnetic circuit parameters, flux density, and uniformity. The impact of various magnetic circuit parameters on magnetic field strength is then analyzed using COMSOL software, which identifies optimal parameters for the stacked structure, resulting in a 9% improvement in magnetic field uniformity. Impedance analysis experimentally validates these results. The optimized stacked magnetic circuit for GMM shows a larger impedance circle diameter, an improved mechanical quality factor, and 95% magnetic field uniformity. By appropriately arranging the bias magnetic field and fine-tuning the magnetic circuit structure, magnetic flux density and uniformity along the GMM rod's central axis are enhanced, reluctance is reduced, and magnetic flux leakage is minimized in the closed magnetic circuit, which ensures high energy conversion efficiency in high-power ultrasonic vibration systems. The study provides essential guidance for optimizing system design and offers valuable insights to improve system efficiency and performance significantly.

Keywords: Magnetostrictive transducer; Energy conversion; Magnetic field uniformity; COMSOL simulation

1 Introduction

Rotary ultrasonic machining (RUM) is extensively employed in mechanical processing, offering an efficient method for machining brittle materials by combining ultrasonic vibration with traditional cutting techniques, which is particularly effective for materials such as optical glass, sapphire crystal, and ceramic matrix composites, as it significantly reduces cutting force while improving surface quality and processing efficiency[1–3]. The most notable impact is seen in milling and drilling applications. Traditionally, piezoelectric transducers are used in RUM to generate ultrasonic vibration, but they can be replaced by giant magnetostrictive ultrasonic transducers (GMUT) due to their larger expansion coefficient, higher energy density, greater ample power capacity, and fast response speed at equivalent power and size[4–6]. GMUT converts alternating current into mechanical energy through the magnetostrictive effect, generating ultrasonic vibrations that produce displacement and force, enabling tools to vibrate at ultrasonic frequencies for material removal from workpieces. Magneto-striction works by modulating the magnetic domains in giant magnetostrictive materials (GMM) under an external magnetic field. As the field fluctuates, GMM deforms, translating magnetic energy into mechanical energy. The mechanical output of GMUT is primarily dependent on the magnetic field distribution within GMM.

The magneto-mechanical-thermal multi-field coupling energy conversion model of GMM has garnered significant research interest in the domain of high-power ultrasonic vibration processing[7,8]. Current investigations into the dynamic properties of GMUT primarily focus on frequency tracking control[9], bias magnetic field configuration[10,11], hysteresis loss modeling[12], and prestress regulation within ultrasonic systems[13]. Numerous experimental results have demonstrated a pronounced nonlinear electromagnetic-thermal coupling between the transducer's input current and output displacement, which severely impacts the vibration behavior of the GMM rod[14–16]. The magnetic circuit generates the driving magnetic field necessary for the GMM rod's high-frequency expansion and

*Corresponding author: (E-mail: yangrui20161118@163.com)

contraction, and its magnetic performance is intricately linked to the circuit's structural parameters, directly influencing the mechanical vibration output of the transducer[17]. In a non-uniform magnetic field, the GMM exhibits high-order harmonic output and suffers material degradation due to uneven tension and compression among magnetic domains. Thus, magnetic field strength uniformity is critical in transducer performance. Most research on transducer magnetic fields has concentrated on the design of drive coils, bias magnetic field selection, and the use of magnetic conductors to create closed magnetic circuits to increase magnetic field intensity[10,18–20]. However, limited attention has been given to improving the uniformity of magnetic field strength and optimizing magnetic field utilization within the closed magnetic circuit. A systematic design methodology and theoretical framework for these improvements have yet to be established. Furthermore, magnetic circuit design predominantly relies on finite element analysis, with scant exploration of how key structural parameters of magnetic conductors can enhance field performance. Experimental studies addressing the reduction of magnetic leakage, enhancement of magnetic field strength, and improvement of magnetic field uniformity remain sparse.

The paper aims to improve the energy conversion efficiency of the transducer from the perspective of optimizing the magnetic field. Based on the mathematical model of the magnetic circuit and Comsol finite element simulation, the influence of the structural parameters of each component of the magnetic circuit on the magnitude and uniformity of the magnetic field intensity was theoretically analyzed and simulated, and the energy efficiency under various working conditions was compared experimentally. A transducer prototype was developed, and simulations and experiments were carried out to compare the energy efficiency under different working conditions.

2 The structure and working principle of the ultrasound system

Figure 1 illustrates the schematic structure of a typical ultrasound system. The basic configuration includes the magnetic drive mechanism of GMM, the permanent magnet, the magnetic sheet, the magnetic ring, the magnetic sleeve, the excitation coil, the non-contact power system, and the horn. The operational principle entails the transmission of alternating current through the driving coil, thereby engendering an oscillating magnetic field while concurrently harnessing the static magnetic field generated by the permanent magnet to eliminate the frequency-doubling effect. As the excitation current changes, it affects the strength of the magnetic field surrounding the GMM. This causes no linear magnetostriction and promotes the movement of the ejector rod for force and displacement output, ultimately transforming electromagnetic energy into mechanical energy. When the driving magnetic field aligns with the bias magnetic field generated by the permanent magnet, the synthetic magnetic field strengthens, resulting in a positive displacement output from GMUT. Conversely, when the driving magnetic field opposes the direction of the bias magnetic field, the synthetic magnetic field becomes smaller than that of the bias magnetic field, leading to a negative displacement output from GMUT. Therefore, the axial size of the GMM will constantly change due to its magnetostrictive effect. The pre-tightening force is applied by the bolt and magnetic ring. The AC signal transmitted by the non-contact power system causes vibration excitation in the GMM, which is then amplified by the horn's vibration structure unit. The unique fixture is used for attaching the tool to the end of the horn to perform various ultrasonic vibration machining. The spindle of the machine tool combines traditional rotary processing with ultrasonic vibration to achieve high-speed rotation.

3 The analysis of the magnetic circuit

3.1 The structure diagram of the magnetic circuit

The magnetic circuit of the GMUT can be simplified as a closed loop comprising the magnetic drive

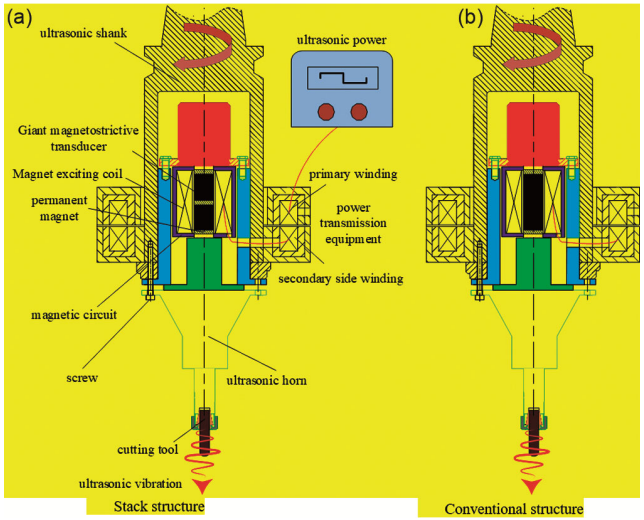

Fig. 1 — The structure of the ultrasound system

mechanism (GMM), permanent magnet, magnetic sheet, magnetic ring, magnetic sleeve, and excitation coil. Given the large diameter of the GMM rod, a stacked bias structure is employed, in which the permanent magnet and GMM are alternately arranged. The configuration enhances the strength of the bias magnetic field while mitigating magnetic flux leakage. The diagram of the magnetic circuit structure is shown in Fig. 2.

3.2 Mathematical model of magnetic circuits

Modeling plays a crucial role in the design and analysis of cost-effective and operationally efficient GMUT systems. The key aim in developing and optimizing a mathematical model for the magnetic circuit is to maximize the magnetization of the GMM rod, enhance the uniformity of the magnetic field, minimize magnetic leakage and energy losses, and improve the output displacement of the GMUT. By defining the partial derivative as the magnetostrictive parameter, the linear constitutive equation of the GMM can be derived by[7]

$$\mathrm{d}S = \left.\frac{\partial S}{\partial T}\right|_H \mathrm{d}T + \left.\frac{\partial S}{\partial H}\right|_T \mathrm{d}H \quad \ldots (1)$$

$$\mathrm{d}B = \left.\frac{\partial B}{\partial T}\right|_H \mathrm{d}T + \left.\frac{\partial B}{\partial H}\right|_T \mathrm{d}H \quad \ldots (2)$$

The simplified piezomagnetic equation is derived by assuming that only the axial stress in the GMM is non-zero, while the effects of transverse and shear stresses are neglected.

$$S_3 = s_{33}^H T_3 + d_{33} H_3 \quad \ldots (3)$$

$$B_3 = d_{33} T + \mu_{33}^T H_3 \quad \ldots (4)$$

$$S_3 = \left(S_{33}^H - \frac{d_{33}^2}{\mu_{33}^T} \right) T_3 + \frac{d_{33}}{\mu_{33}^T} B_3 \quad \ldots (5)$$

Where $S_3, B_3, T_{33}, H_3, d_{33}, S_{33}^H$ 和 μ_{33}^T represent the strain, flux density, stress, magnetic field strength, field coupling coefficient, compliance coefficient, and permeability of the GMM rod in the axial direction, respectively, S_3, d_{33}, S_{33}^H 和 μ_{33}^T are material-dependent parameters. If material variations are disregarded, these parameters can be treated as constants. When T_{33} is specified, the GMM strain S_3 exhibits a linear relationship with the magnetic flux density B_3. The internal magnetic flux density of the GMM directly influences the magnetostrictive effect, with a higher flux density leading to a greater magnetostrictive strain. Thus, to improve the output performance of the GMUT, it is essential to maximize and homogenize the internal flux distribution.

By applying Gauss's law for magnetic flux and Kirchhoff's law, the magnetic circuit equation can be derived, reflecting the conservation of magnetic flux and the balance of potential differences in a closed-loop magnetic circuit.

$$F = NI = \Phi R = B A_g \left(R_g + R_p \right) \quad \ldots (6)$$

$$A_g = \pi (r_{g2}^2 - r_{g1}^2) \quad \ldots (7)$$

Where F is the magnetomotive force, N is the number of turns of the coil, I is the coil current, Φ is the total flux of the magnetic circuit. $R$is the total reluctance in the magnetic circuit, R_g is the reluctance of the GMM, and R_P is the reluctance of the external

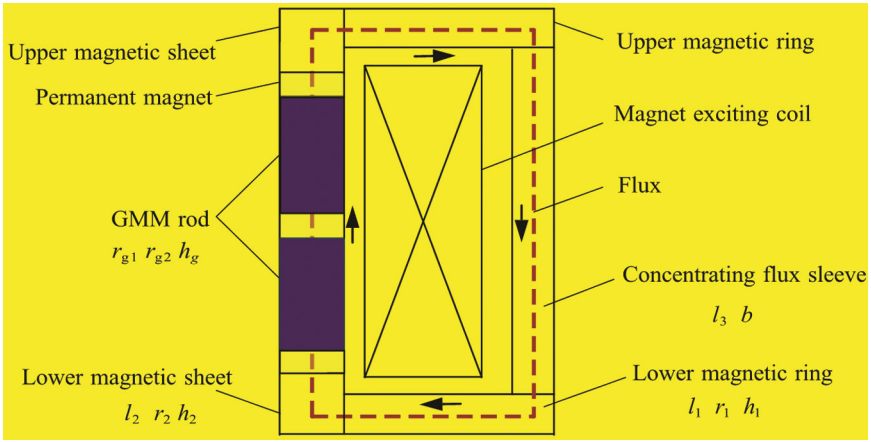

Fig. 2 — The structure diagram of the magnetic circuit

magnetic circuit. *B*is the magnetic flux density. A_g represents the cross-sectional area of the GMM. The structure diagram of the GMM is shown in Fig. 3.

In conjunction with the structure of the GMM, the reluctance of the external magnetic circuit and the reluctance of the GMM can be expressed as corresponding functions of the geometric dimensions and material properties, accounting for the magnetic path and permeability of each component.

$$R_g = \frac{\pi}{2\mu h_g} \ln\left(\frac{r_{g2}}{r_{g1}}\right) \quad \ldots (8)$$

$$R_p = \frac{l_p}{u_0 u_p A_p} \quad \ldots (9)$$

Where h_g and μ represent the length and relative permeability of the GMM rod, respectively; r_{g2} and r_{g1} are the large and small diameters of the GMM rod, respectively; $\mu_0$is the vacuum permeability; l_p, μ_p and A_P are the effective length, relative permeability, and equivalent cross-sectional area of the external magnetic circuit, respectively. Assuming that the magnetic flux leakage of the coil is negligible, it can be considered that all magnetic field lines pass through the GMM. The magnetic flux density can subsequently be determined by combining Eqs. (6), (8), and (9).

$$B = \frac{NI}{A_g R} = \frac{NI}{A_g\left(R_g + R_p\right)} \quad \ldots (10)$$

According to Eq. (10), when N、I, and A_g are constant, the axial magnetic flux density B of the GMM rod is inversely proportional to the total magnetic reluctance R of the circuit. Hence, to enhance the magnetic flux density B under a given driving magnetic field, it is essential to reduce the total magnetic reluctance. As indicated by Eq. (9), once the GMM rod is fixed, the reluctance of the external magnetic circuit can be minimized by maintaining the R_g constant. When the equivalent cross-sectional area and effective length of the external magnetic circuit R_p remain unchanged, increasing the relative permeability of the external magnetic circuit material lowers its magnetic reluctance. Therefore, industrial pure iron, with its high magnetic permeability, is utilized as the material for the GMA's external magnetic circuit.

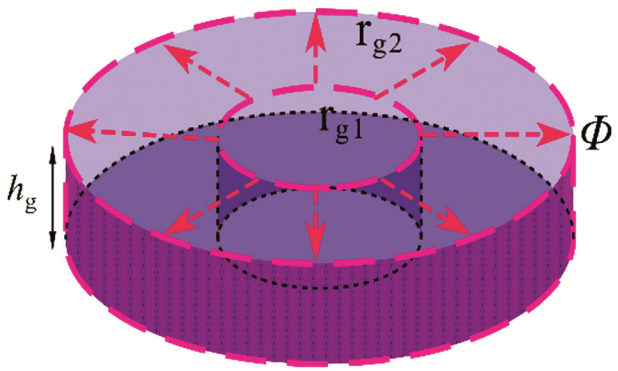

Fig. 3 — Cross-sectional analysis of the GMM rod ring

3.3 Theoretical analysis of magnetic circuit parameters

The magnetic circuit model in Fig. 4 is constructed based on the GMA structure shown in Fig. 1. In this model, *NI* represents the magnetomotive force generated by the driving coil. φ_1 corresponds to the magnetic flux in the closed magnetic circuit of the GMA, while φ_2 represents the magnetic flux in the air forming a closed loop. Since the GMUT is axisymmetric and both the upper and lower magnetic rings, as well as the magnetic sheets, are made of the same material, R_{p1}, R_{p2}, R_{p3}, and R_{p4} denote the equivalent magnetic resistances of the upper and lower magnetic rings, magnetic sheets, magnetic sleeve, and output rod, respectively, while the air gap magnetic resistance between components is neglected. R_{p5} represents the magnetic resistance of the air surrounding the GMUT.

The GMUT can be simplified into a closed magnetic circuit composed of the GMM rod, upper and lower magnetic rings, upper and lower magnetic

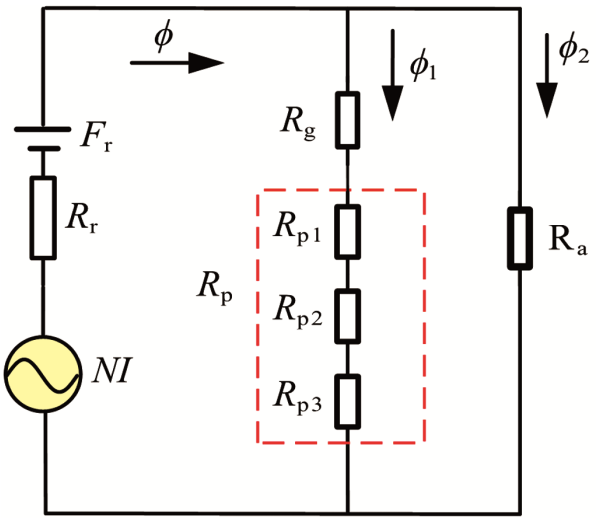

Fig. 4 — The equivalent magnetic circuit of a giant magnetostrictive transducer

sheets, the magnetic sleeve, and the output rod. The magnetomotive force within the GMM is described by Eq. (6) and the continuity of magnetic flux is expressed as follows:

$$F = NI = H_g l_g + H_1 l_1 + H_2 l_2 + H_3 l_3 + H_4 l_4 \quad \ldots (11)$$

Where, H_g represents the average magnetic field intensity along the central axis of the GMM rod. H_1, H_2, H_3 and H_4 denote the average magnetic field intensities in the upper and lower magnetic rings, upper and lower magnetic sheets, magnetic sleeve, and output rod, respectively. Correspondingly, l_1, l_2, l_3, and l_4 are the effective lengths of the upper and lower magnetic rings, upper and lower magnetic sheets, magnetic sleeve, and output rod, respectively.

Since the total magnetic flux ϕ in the closed magnetic circuit of the GMUT is continuous, the following relationship holds among the various components of the magnetic circuit:

$$\mu_g H_g A_g = \mu_1 H_1 A_1 = \mu_2 H_2 A_2 = \mu_3 H_3 A_3 = \mu_4 H_4 A_4 \quad \ldots (12)$$

Where μ_1、 μ_2、 μ_3 and μ_4 represent the relative magnetic permeabilities of the upper and lower magnetic rings, upper and lower magnetic sheets, magnetic sleeve, and output rod, respectively. Additionally, A_1、A_2、$A_3$and A_4 denote the equivalent cross-sectional areas of the upper and lower magnetic rings, upper and lower magnetic sheets, magnetic sleeve, and output rod, respectively.

By combining Eqs (11) & (12), the magnetic field intensity along the central axis of the GMM rod can be expressed by the following equation:

$$H_g = \frac{NI}{l_g + \frac{\mu_g A_g l_1}{\mu_1 A_1} + \frac{\mu_g A_g l_2}{\mu_2 A_2} + \frac{\mu_g A_g l_3}{\mu_3 A_3} + \frac{\mu_g A_g l_4}{\mu_4 A_4}} \quad \ldots (13)$$

Where $A_g = \pi(r_{g2}^2 - r_{g1}^2)$, $A_1 = \pi\left(r_1^2 - r_2^2\right)$, $A_2 = \pi\left(r_2^2 - r_{g1}^2\right)$, $A_3 = \pi\left[r_1^2 - (r_1 - b)^2\right]$

It can be observed that when the GMM is selected, μ_g、 A_g and l_g are constants. For constant N and I, the magnetic field intensity H_g affecting the central axis of the GMM rod is influenced by the radiusr_1 of the upper magnetic ring, the radius r_2 of the lower magnetic sheet, the thicknessh_1 of the upper magnetic ring, the thickness h_2 of the lower magnetic sheet, and the thickness b of the magnetic sleeve.

4 Finite element analysis of the magnetic field

4.1 Establishment of finite element model of magnetic field

As illustrated by the GMUT structural model in Fig. 1, the magnetic circuit of the GMUT exhibits a 3D axisymmetric configuration, allowing for simplification and subsequent modeling within Comsol. Comsol, serving as a finite element analysis tool, is employed to conduct finite element simulations on the GMUT magnetic circuit. The magnetic field intensity and its uniformity along the central axis of the GMM rod are used as criteria to assess the performance of the magnetic circuit. The uniformity of the magnetic field intensity can be expressed as:

$$\zeta = \left(1 - \frac{H_{max} - H_{min}}{H_{max}}\right) \times 100\% = \frac{H_{min}}{H_{max}} \quad \ldots (14)$$

Where H_{max} and H_{min} are the maximum and minimum magnetic field strengths on the central axis of the GMM rod.

The model is established and material properties are defined within the finite element software Comsol, with the coil excitation source specified by the NI value. The model is meshed, ensuring the maximum grid side length does not exceed 3 mm to maintain computational accuracy, with the excitation voltage set to 60V. Due to the axisymmetric nature of the transducer, planar axisymmetric elements are utilized in the solution. The GMM rods are modeled using PLANE13 elements. The grid configuration is illustrated in Fig. 5. The relevant parameters of the GMUT drive magnetic circuit model materials are shown in Table 1.

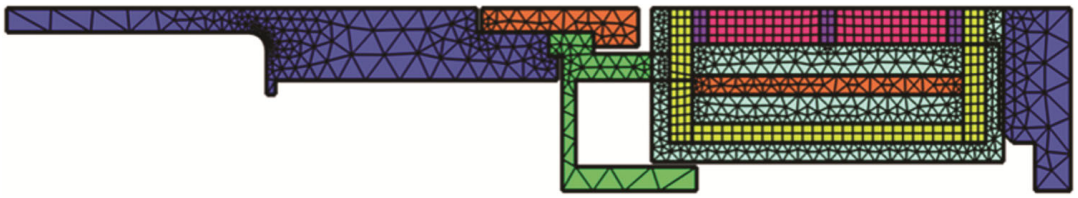

Fig. 5 — Finite element mesh division

4.2 Influence of magnetic circuit structure parameters on the magnetic field

Figure 6 depicts the magnetic flux density and its uniform distribution along the strain direction of the GMUT, revealing significant uniformity in the magnetic field across the GMM. Furthermore, simulations of the magnetomotive force and magnetic flux density within the GMM have been conducted, with the results shown in Fig. 7.

Table 1 — The parameters of model materials

Name	Value	Name	Value
Diameter of GMM /mm	25	Coil turn	350
Length of GMM /mm	20	Coil Length /mm	180
The relative magnetic permeability of GMM	7.3	Peak voltage /V	60
Relative permeability of industrial pure iron	11947	Wire radius r/mm	1.2

Figure 7 shows that the magnetic flux density is predominantly concentrated around the magnetic poles, with the magnetic field lines passing uniformly through the GMM rods. The peak magnetic flux density along the central axis of the two GMM rods reaches 2.29 T, indicating a relatively strong magnetic field and improved uniformity in the flux distribution. This can be attributed to the use of high-permeability materials in the magnetic circuit, which reduces air magnetoresistance, minimizes magnetic leakage losses, increases the magnetic flux utilization rate, and

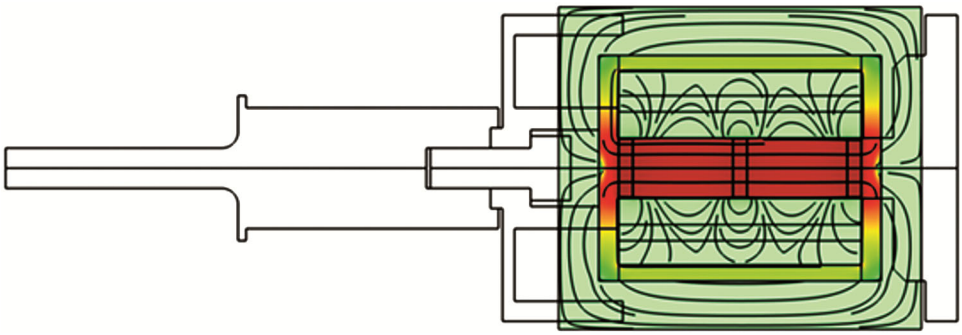

Fig. 6 — The magnetic flux density

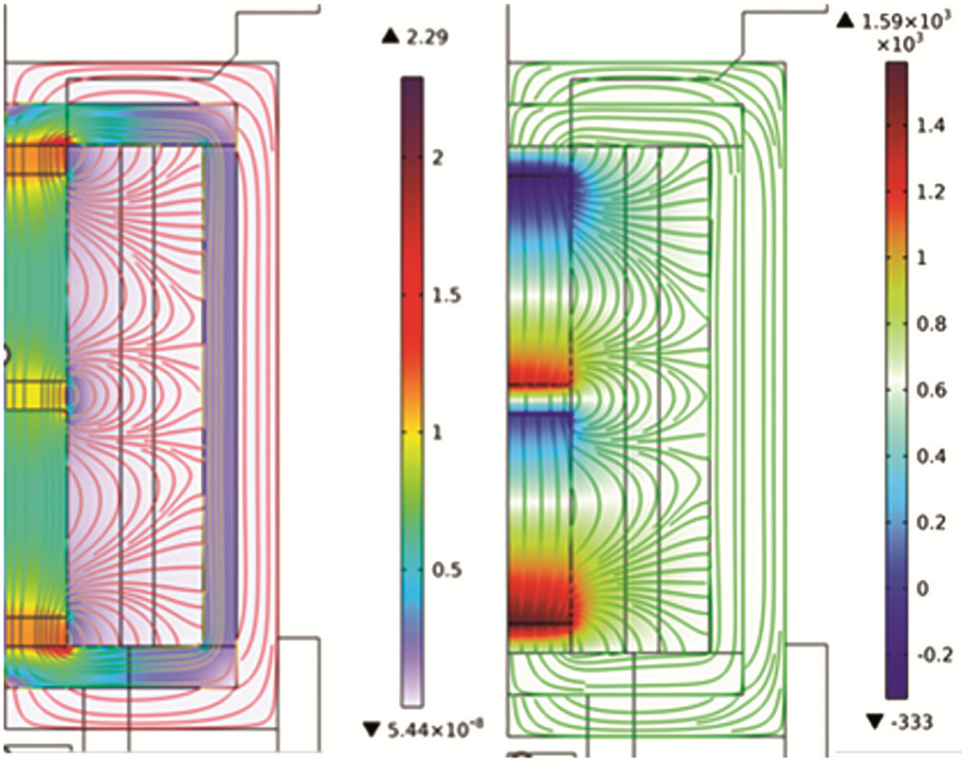

Fig. 7 — The magnetic field strength of GMM

ultimately enhances energy conversion efficiency. A further analysis of the external magnetic circuit structure is conducted to investigate the influence of magnetic circuit structural parameters on the magnetic field.

The effects of varying the magnetic ring thicknessl_1, ring radiusr_1, sheet thickness l_2, sheet radiusr_2, sleeve thickness b, and the axial length l of the drive coil on the magnetic field intensity along the central axis of the GMM rod are simulated sequentially. Upon completing the simulation, a segment of the GMM rod is chosen for magnetic field intensity analysis. The corresponding results are displayed in Fig. 8.

4.3 The analysis of simulation results

4.3.1 The effect of the magnetic ring on the magnetic field intensity

As depicted in Fig. 9(a & b), when the inner radius of the magnetic sleeve is 24 mm and the thickness of the magnetic sleeve increases with the magnetic ring radius, the maximum magnetic field intensity along the central axis of the GMM rod initially rises and then reaches saturation as the magnetic ring's thickness and radius increase. This occurs because the expanding thickness and radius reduce the magnetic flux leakage at the end of the driving coil, thereby enhancing the magnetic flux along the GMM rod′s central axis. However, further increases in the

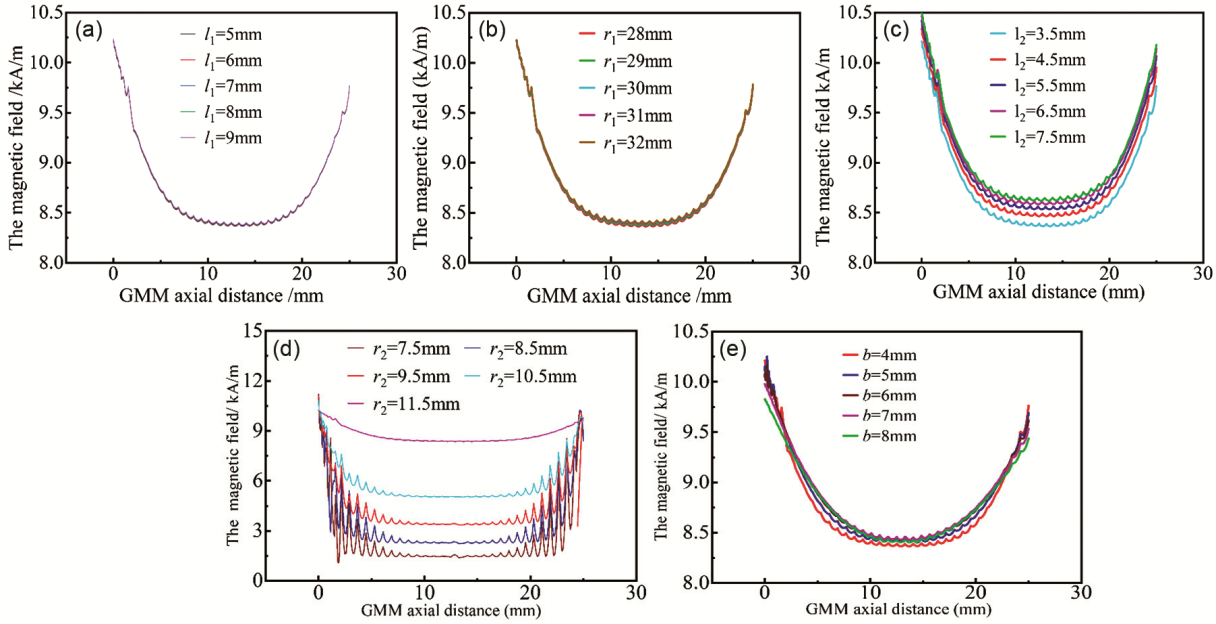

Fig. 8 — The influence of the magnetic circuit structure parameters on the magnetic field strength; a, b, c, d, and e respectively represent the effects of magnetic ring thickness, magnetic ring radius, magnetic sheet thickness, magnetic sheet radius, and magnetic sleeve thickness on the GMM magnetic field intensity distribution

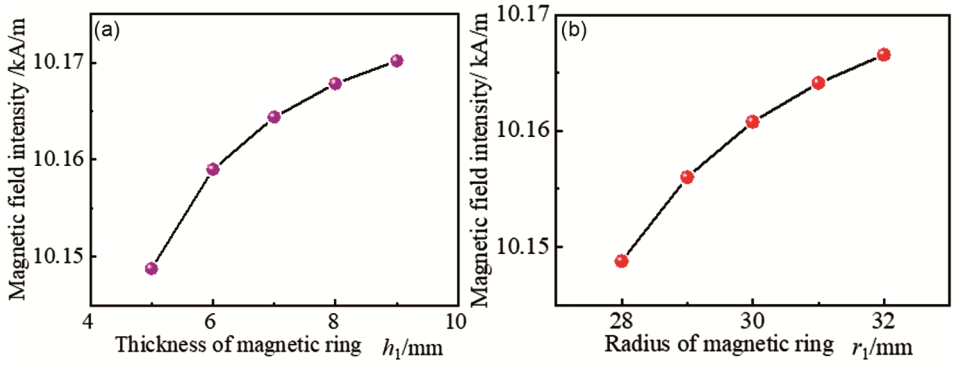

Fig. 9 — Influence of magnetic flux ring on the central axis magnetic field of GMM rod: (a) Thickness of magnetic ring; (b) radius of magnetic ring

magnetic ring′s dimensions lead to diminishing effects on leakage reduction until saturation is reached. Thus, selecting an optimal thickness and radius for the magnetic ring is crucial for minimizing magnetic leakage and maximizing magnetic field intensity. When the magnetic field intensity reaches its peak, as shown in Fig. 9(a & b), the magnetic ring has a thickness of 9 mm, a radius of 32 mm, and the magnetic sleeve has a thickness of 11 mm.

4.3.2 The influence of magnetic sheet on the magnetic field intensity

As shown in Fig. 10(a), the magnetic field intensity along the central axis of the GMM rod initially increases and then decreases with the rising radius of the magnetic sheet. This occurs because a larger radius reduces the magnetic resistance at the end of the GMM rod, drawing the magnetic field closer to the centre. However, further increases in radius lead to a decline in magnetic field intensity due to the dispersion effect. In Fig. 10(b), as the thickness of the magnetic sheet increases, the magnetic field intensity on the central axis also rises. A thicker magnetic sheet reduces magnetic resistance at the GMM rod's end, thereby boosting the magnetic field intensity. The greater the thickness, the smaller the magnetic resistance, leading to improved field uniformity near the centre. Consequently, when the magnetic field intensity reaches its peak, the optimal magnetic sheet thickness is 7.5 mm, with a radius of 8 mm.

5 Simulation and experimental results verification

Based on the aforementioned theory and finite element analysis, the optimal dimensions for the external magnetic circuit structure are determined as l_1=9mm, r_1=32mm, l_2=7.5mm, r_2=8mm, and b=8mm. The magnetic circuit simulation results corresponding to these optimal dimensions are presented in Fig. 11.

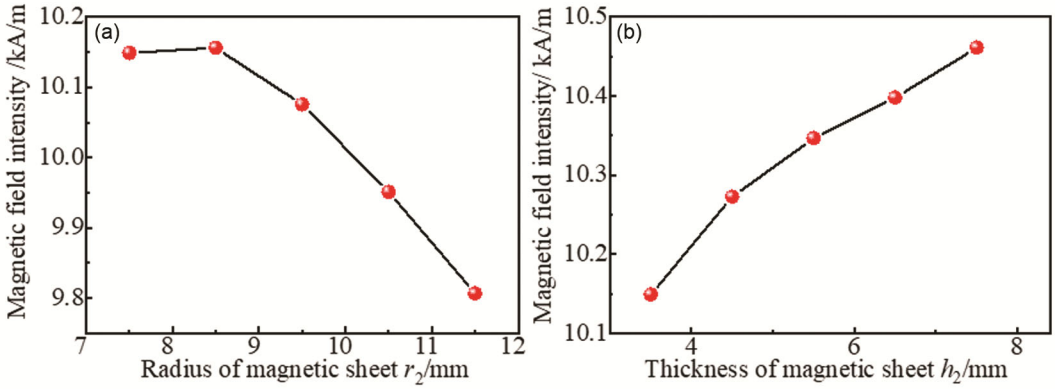

Fig. 10 — The influence ofthe magnetic sheet on the magnetic field strength of the central axis: (a) the radius of the magnetic sheet;(b) the thickness of the magnetic sheet

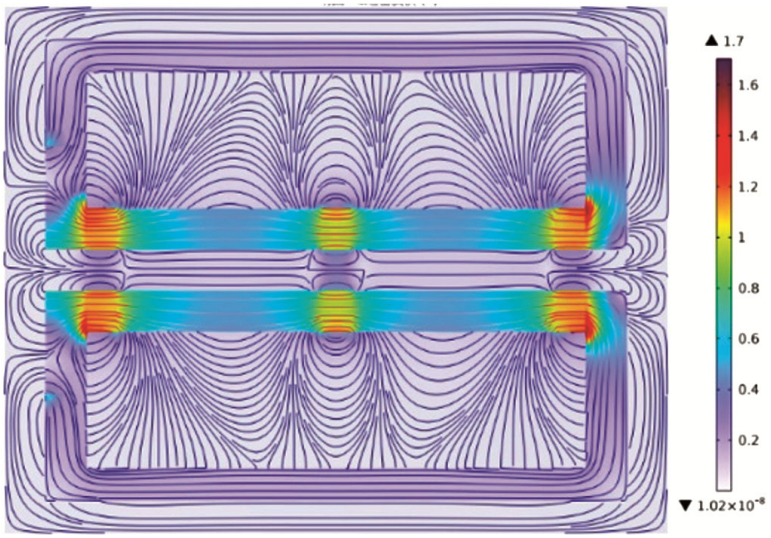

Fig. 11 — The axial magnetic field uniformity of GMM rod

Fig. 11 illustrates that the magnetic field exhibits good uniformity, and the magnetic flux density is high. To quantitatively assess the uniformity of the magnetic field, the concept of magnetic field inhomogeneity is introduced to analyze the model's magnetic field. It can be expressed as follows.

$$\eta = \frac{\sqrt{\frac{1}{n}\sum_{i=1}^{n}(H_i - H_{avg})^2}}{H_{avg}} \times 100\% \quad \ldots (15)$$

Where H_i represents the magnetic field intensity at the i-th point, and H_{avg} denotes the average magnetic field intensity at the selected points. By selecting arbitrary points along two segments of the GMM, the magnetic field inhomogeneity at these locations is calculated to be approximately 5%. Thus, the magnetic field uniformity of this structure reaches 95%. Compared to previous studies[21], this represents a 9% improvement in uniformity. Therefore, to balance processing efficiency and performance, a two-level stacking structure is employed to further enhance the magnetic field uniformity of the GMM, meeting the necessary application requirements.

To better demonstrate the advantages of the stacked structure, a comparison experiment on impedance characteristics was conducted using the optimized magnetic circuit parameters and the traditional single-rod transducer. The impedance performance of the GMM single-rod and stacked transducers was evaluated through an impedance analysis experiment, as illustrated in Fig. 12.

In addition, the electromechanical conversion factor of the two magnetostrictive transducers of the Terfenol-D rod can be expressed as

$$r = 2m\pi\left(f_2 - f_1\right) \quad \ldots (16)$$

$$T_{me} = \sqrt{\left(\left|Z_{mot}\right|\right)r} \quad \ldots (17)$$

Where r is the equivalent impedance, f_1 and f_2 are the half-power frequencies, and Z_{mot} is the impedance circle diameter.

The impedance analysis results are shown in Table 2. As shown in Fig.12 and Table 2, a significant difference in the resonant frequencies between the two structures is observed. The impedance circle diameter of the stacked structure is notably larger, indicating better magnetic flux uniformity, higher magnetic permeability, reduced magnetic flux leakage, and enhanced conversion efficiency of the ultrasonic vibration system.

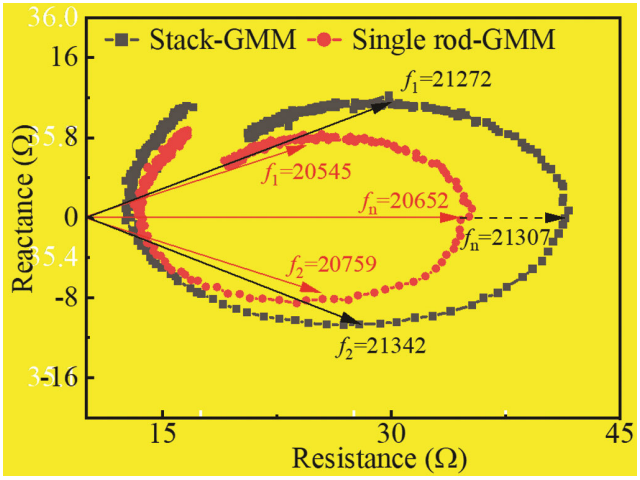

Fig. 12 — Comparison of transducer impedance performance

Table 2 — Impedance test results of two transducers

Name	Single rod-GMM	Stack-GMM
Resonance frequency/ Hz	20652	21307
Half-power frequency/ Hz	20545 20759	21272 21342
Impedance circle diameter/Ω	23	28
Electromechanical conversion factor	30.8	45.6

6 Conclusion

The paper presents a theoretical analysis of the magnetic field in a stacked giant magnetostrictive transducer, supplemented by numerical simulations using the finite element method.

(1) The findings indicate that the magnetic ring and sleeve primarily function to minimize magnetic leakage and enhance magnetic field intensity. As the thickness and radius of the magnetic ring and sleeve increase, the maximum magnetic field strength along the GMM rod's central axis initially rises before reaching saturation. Additionally, the magnetic sheet plays a crucial role in improving the uniformity of the magnetic field strength along the central axis, with uniformity increasing and subsequently saturating as the radius and thickness of the magnetic sheet grow.

(2) Finite element analysis was employed to investigate the optimal dimensions of the external magnetic circuit identified through simulations. The results indicated that the magnetic field uniformity attained 95%, representing a 9%

improvement over previously reported values in the literature[21]. The stacked structure effectively reduces magnetic leakage from the transducer, thereby enhancing its energy conversion efficiency. This study also included an impedance analysis, revealing that the GMM stacked structure possesses a larger impedance circle diameter and a higher mechanical quality factor compared to the single-rod structure.

This magnetic circuit design strategy enables control with reduced inductance, allowing the ultrasonic system to achieve a significantly greater ultrasonic vibration gain in a fully resonant state. Such advancements facilitate high-quality ultrasonic vibration processing and provide critical insights for the design of high-power ultrasonic vibration systems.

Declaration of Competing Interest

The authors declare that they have no known competing financial interests or personal relationships that could have appeared to influence the work reported in this paper.

Acknowledgements

This work was supported by the Key Scientific Research Projects of Universities in Henan Province (No. 25B460017).

References

1 Ma K, Wang J, Zhang J, Feng P, Yu D & Ahmad S, *Int J Mech Sci*, 214 (2022) 106927.
2 Cao J, Nie M, Liu Y & Li J, *Int J Adv Manuf Technol*, 96 (2018) 3251.
3 Lan T, Feng P, Zhang J, Zhou H & Wang J, *Int J Mech Sci*, 246 (2023) 108136.
4 Zhou H, Zhang J, Feng P, Yu D, Wu Z, *Ultrasonics*, 108 (2020) 106017.
5 Yang Z, Zhu L, Zhang G, Ni C & Lin B, *Int J Mach Tools Manuf*, 156 (2020) 103594.
6 Deng Y, Zhang G & Zhang X, *Appl Acoust*, 158 (2020) 107066.
7 Jin K, Kou Y & Zheng X, *J Magn Magn Mater*, 324 (2012) 1954.
8 Zheng X J & Sun L, *J Appl Phys*, 100 (2006) 063906.
9 Lan T, Feng P, Zhang J, Zhang X & Wang J, *Mech Syst Sig Process*, 210 (2024) 111193.
10 Yang M, Yang X & Wei Y, *IEEE Trans Ultrason Ferroelect Freq Contr*, 69 (2022) 812.
11 Li H, Gao B, Yang M, Yang W, Wu Z & Zhao N, *IEEE Sensors J*, 24 (2024) 10257.
12 Xu H, Pei Y, Fang D & Ai S, *Int J Solids Struct*, 50 (2013) 672.
13 Zhu Y, Yang X & Wereley N M, *Smart Mater Struct*, 25 (2016) 085030.
14 Xie T, Wang C, Yu C, Xu B & Shi R, *AIP Adv*, 10 (2020) 105126.
15 Chen L, Zhu Y, Ling J & Zhang M, *Appl Therm Eng*, 230 (2023) 120736.
16 Li Y, Dong X & Yu X, *Micromachines*, 14 (2023) 1103.
17 Yang Z, He Z, Li D & Rong C, *Adv Mater Sci Eng*, 2016 (2016)1.
18 Xue G, He Z, Li D, Yang Z & Zhao Z, *J Magn Magn Mater*, 394 (2015) 416.
19 Li S X, Yang X, Chen Z K & Chen Y K, *Trans Chin Electrotechnical Soc*, 38 (2023) 2277.
20 Tang Z, Lü F & Liu Y, *J Rare Earths*, 27 (2009) 525.
21 Xu B, Wang C, Wang L, Cheng Y & Yang X, *AIP Adv*, 11 (2021) 045125.